Process–Structure–Property Relationship in FeCoNiAl$_x$Mn$_x$ Complex Concentrated Alloys Processed by Additive Manufacturing

A. Poulia, A.S. Azar, M. Schrade, J.S. Graff, C. Bazioti, A.E. Gunnæs, P.A. Carvalho, and S. Diplas

Fourteen alloys of the FeCoNiAl$_x$Mn$_x$ system were processed by laser metal deposition (LMD). The feedstock was a weighted and proportional blend of the containing elemental powders, targeting the nominal alloy compositions. Prior to processing, the composition and particle characteristics of the feedstock were assessed. The microstructural features and crystal structures of all LMD processed materials were characterized with scanning electron microscopy/energy dispersive spectroscopy and x-ray diffraction, in both as-received and heat-treated conditions. Selected samples were investigated via scanning transmission electron microscopy and electron backscattered diffraction for further structural understanding. Hardness tests, under various indentation loads and dwelling times, were performed to assess the mechanical properties of the processed samples. The results showed a rise in hardness as Al and Mn contents increase. The variation of hardness with composition follows a reverse sigma-type curve, reflecting the microstructural evolution and grain size variations in the alloys. Based on the hardness data, we suggest a trained and validated predictive model, which can be used in alloy design for future developments.

1. Introduction

The development of new design strategies for metallic alloys is a persistent, yet critical issue in materials science (Ref [1]). The concept of high entropy alloys (HEA) has significantly contributed to transforming the so far traditional view of metallic materials (Ref [2]). By definition, HEAs consist of at least five principal elements, with each one at a concentration between 5 and 35 at.% (Ref [3]). During the last years, HEAs have attracted considerable scientific attention, mostly due to an unprecedented combination of microstructural features, such as simple solid solutions (fcc, bcc or hcp), nanocrystalline, amorphous phases, mesophases or other complex phases (Ref [4]). These features have resulted in most cases to a unique combination of intriguing properties, such as good structural stability, remarkable combinations of strength/hardness and ductility, exceptional wear resistance, good corrosion/oxidation response, often along with interesting functional properties

including electrical, magnetic and hydrogen storage applications (Ref [5-7]). This new class of materials broadened the synthesis limits by enabling the production of a wide range of microstructures associated with properties and new application areas currently unexplored by conventional materials (Ref [8]).

In recent studies, HEAs do not only refer to single-phase solid solution microstructures. A wider and more flexible range of compositions has gradually been selected, giving rise to what is commonly referred as complex concentrated alloys (CCA), multi-principal element alloys (MPEA) or simply 'baseless' alloys (Ref [9]). The range of these materials' structures and properties has extensively been analyzed in numerous studies (Ref [10]). In brief, alloy families of 3d transition metal CCAs or refractory metal CCAs exhibit amorphous, nanocrystalline, single-phase or multi-phases, while combining properties that may differ from those of conventional alloys. Many refractory CCAs can potentially compete with nickel superalloys offering increased operating stress and temperature conditions, as well as thermal expansion, conductivity, and diffusivity values similar to those of highly alloyed steels and superalloys.

Additive manufacturing technologies provide opportunities in blending various elemental and/or alloy powders and have therefore become methods of choice to create new alloy compositions through in situ alloying (Ref [11-14]). There has been a pronounced activity to use theoretical and computational models to predict multi-component structures. However, simple criteria able to consistently predict the formation of intermetallic phases and/or secondary solid solutions have not yet been established. As of today, there have not been globally established criteria to verify HEAs containing either intermetallic phases and/or single solid solutions (Ref [15]). Even so, these models proved to be helpful tools in alloy design and composition selection, targeting to the respective desirable phases and properties.

Further studies assessing process–structure–property relationships as well as focusing on the development of predictive

A. Poulia, C. Bazioti, and **A.E. Gunnæs**, Department of Physics, University of Oslo, Oslo, Norway; and **A.S. Azar, M. Schrade, J.S. Graff, P.A. Carvalho,** and **S. Diplas**, SINTEF Industry, Oslo, Norway. Contact e-mail: am@effee-induction.com.

Table 1 Nominal and obtained compositions (at.%) of the alloys synthesized via LMD and hopper feed of the two batches

| Sample	Nominal composition, at.%	Obtained composition (Dark area), at.%	Obtained composition (Bright area), at.%	Fe-Co-Ni Hopper speed, %	Al-Mn Hopper speed, %
S1	$Fe_{10.9}Co_{10.9}Ni_{10.9}Al_{33.6}Mn_{33.6}$	$Fe_{14.8}Co_{14.7}Ni_{12.9}Al_{29.1}Mn_{28.5}$	$Fe_{22.8}Co_{9.0}Ni_{5.9}Al_{12.6}Mn_{49.7}$	24	68
S2	$Fe_{18}Co_{18}Ni_{18}Al_{23}Mn_{23}$	$Fe_{16.8}Co_{17.9}Ni_{17.9}Al_{26.0}Mn_{21.4}$	$Fe_{22.9}Co_{17.8}Ni_{8.7}Al_{15.4}Mn_{35.2}$	28	61
S3	$Fe_{20.8}Co_{20.8}Ni_{20.8}Al_{18.8}Mn_{18.8}$	$Fe_{18.2}Co_{17.9}Ni_{20.0}Al_{26.1}Mn_{17.8}$	$Fe_{25.7}Co_{16.0}Ni_{12.3}Al_{17.8}Mn_{28.2}$	30	57
S4	$Fe_{22.5}Co_{22.5}Ni_{22.5}Al_{16.2}Mn_{16.2}$	$Fe_{19.2}Co_{18.5}Ni_{21.9}Al_{24.7}Mn_{15.7}$	$Fe_{28.0}Co_{20.9}Ni_{16.8}Al_{12.8}Mn_{21.5}$	31	53
S5	$Fe_{24.2}Co_{24.2}Ni_{24.2}Al_{13.7}Mn_{13.7}$	$Fe_{21.9}Co_{22.4}Ni_{21.5}Al_{19.6}Mn_{14.6}$	$Fe_{28.5}Co_{21.3}Ni_{16.9}Al_{13.7}Mn_{19.6}$	33	50
S6	$Fe_{26.5}Co_{26.5}Ni_{26.5}Al_{10.3}Mn_{10.3}$	$Fe_{23.2}Co_{25.8}Ni_{26.2}Al_{14.2}Mn_{10.6}$	$Fe_{25.3}Co_{24.9}Ni_{22.8}Al_{14.6}Mn_{12.4}$	35	44
S7	$Fe_{27.5}Co_{27.5}Ni_{27.5}Al_{8.8}Mn_{8.8}$	$Fe_{21.9}Co_{24.0}Ni_{23.1}Al_{18.6}Mn_{12.4}$	$Fe_{25.7}Co_{25.2}Ni_{22.4}Al_{12.6}Mn_{14.1}$	36	41
S8	$Fe_{27.9}Co_{27.9}Ni_{27.9}Al_{8.1}Mn_{8.1}$	$Fe_{25.4}Co_{24.2}Ni_{22.5}Al_{16.9}Mn_{11.0}$	$Fe_{26.2}Co_{26.2}Ni_{22.9}Al_{11.6}Mn_{13.1}$	37	40
S9	$Fe_{28.1}Co_{28.1}Ni_{28.1}Al_{7.8}Mn_{7.8}$	$Fe_{28.0}Co_{24.4}Ni_{21.9}Al_{13.8}Mn_{11.9}$	$Fe_{22.3}Co_{22.1}Ni_{26.1}Al_{18.7}Mn_{10.8}$	37	39
S10	$Fe_{28.8}Co_{28.8}Ni_{28.8}Al_{6.8}Mn_{6.8}$	$Fe_{29.7}Co_{26.4}Ni_{21.9}Al_{11.9}Mn_{10.1}$	$Fe_{21.5}Co_{21.7}Ni_{20.5}Al_{19.9}Mn_{16.4}$	38	37
S11	$Fe_{29.4}Co_{29.4}Ni_{29.4}Al_{5.9}Mn_{5.9}$	$Fe_{26.3}Co_{28.6}Ni_{21.7}Al_{14.7}Mn_{8.7}$	$Fe_{17.9}Co_{21.1}Ni_{26.6}Al_{20.7}Mn_{13.7}$	39	35
S12	$Fe_{29.6}Co_{29.6}Ni_{29.6}Al_{5.6}Mn_{5.6}$	$Fe_{26.9}Co_{26.7}Ni_{22.2}Al_{15.3}Mn_{8.9}$	$Fe_{27.3}Co_{27.2}Ni_{25.7}Al_{11.0}Mn_{8.8}$	39	34
S13	$Fe_{31.6}Co_{31.6}Ni_{31.6}Al_{2.6}Mn_{2.6}$	$Fe_{29.9}Co_{28.9}Ni_{28.5}Al_{6.9}Mn_{5.8}$	$Fe_{30.2}Co_{29.8}Ni_{26.9}Al_{8.4}Mn_{4.7}$	43	26
S14	$Fe_{32.3}Co_{32.3}Ni_{32.3}Al_{1.6}Mn_{1.6}$	$Fe_{30.9}Co_{29.9}Ni_{25.2}Al_{8.3}Mn_{5.7}$	$Fe_{31.9}Co_{31.8}Ni_{27.1}Al_{4.7}Mn_{4.5}$	44	23
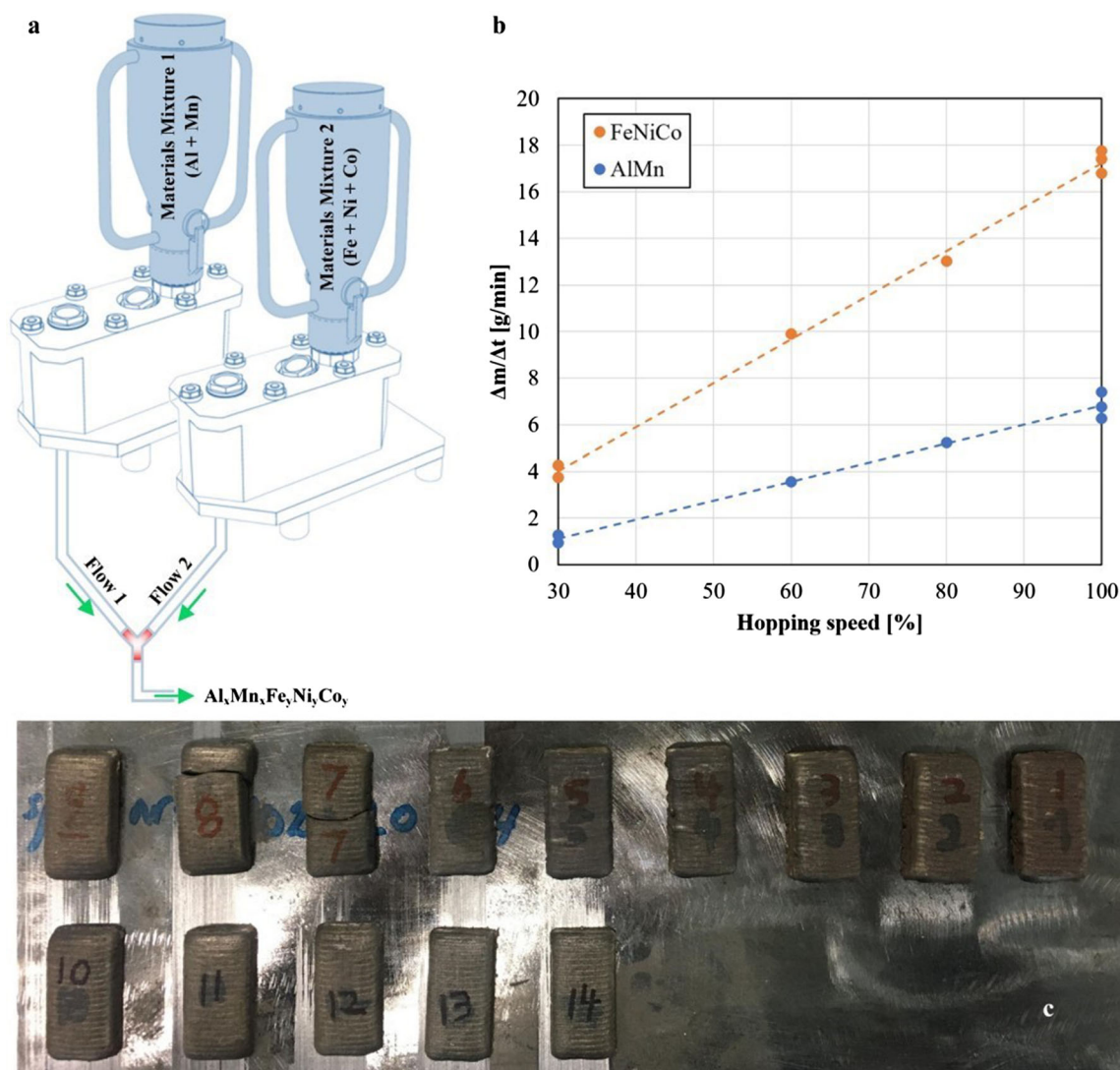
Figure 1 (a) Schematic illustration of the experimental setup of LMD, (b) calibration curves of the hopper system, showing a linear dependency. The nominal composition of the ingot material can be continuously adjusted by running the two hoppers at different speeds and (c) The 14 different FeCoNiAl$_x$Mn$_x$ alloy blocks produced. The samples that are shown broken are due to mishandling under cutting process from the substrate
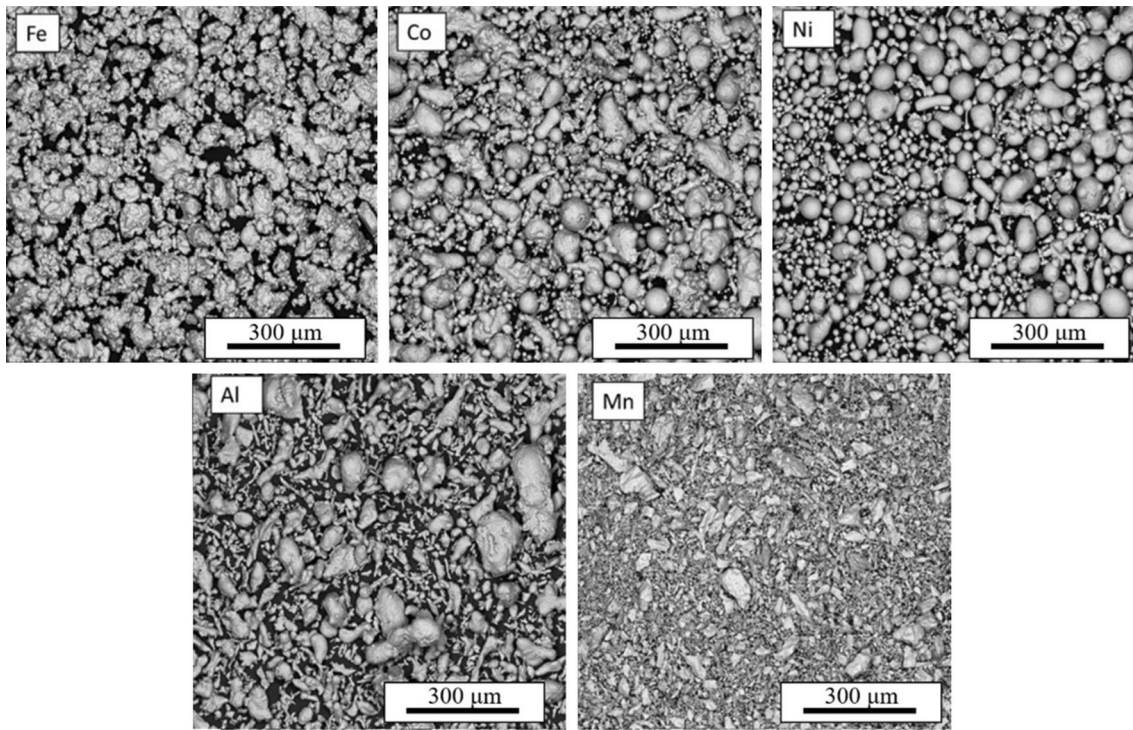
Figure 2 Backscattered electron micrographs of the elemental powders used in the LMD production of the $FeCoNiAl_xMn_x$ system

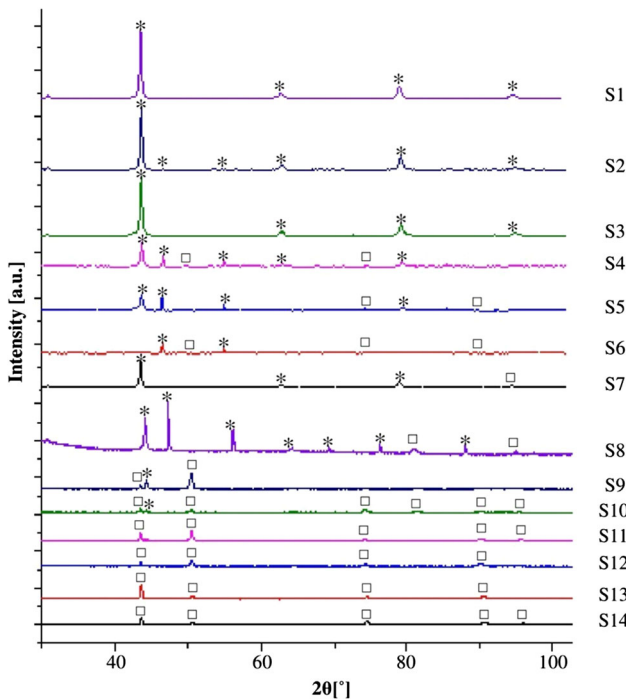**Figure 3** Comparative x-ray diffractograms of the $FeCoNiAl_xMn_x$ alloys synthesized by LMD. The * peaks correspond to an ordered bcc-based lattice, while the □ refer to the common fcc-type structure

models are also important in order to evaluate the processability and applicability of these materials. To puzzle out the key points of constituent phase evaluations in CCAs and connect them with their actual properties, new screening tools and phase evolution theories are also of high demand. In the above

context, the present work is an attempt to correlate the additive manufacturing method of LMD with the produced structure and mechanical properties of various CCAs of the $FeCoNiAl_xMn_x$ system.

2. Experimental Procedure

Elemental powders of Fe, Mn, Co, Ni and Al were characterized for purity and size distribution by analytical scanning electron microscopy (SEM). The powders were sieved using a Retsch AS 200 Control system to remove particles with sizes below 35 μm and above 200 μm, and their stoichiometric amounts were roll mixed to obtain two batches of Al-Mn and Fe-Ni-Co nominal compositions. These batches were loaded in a powder hopper consisting of two separate containers, to feed various blends to the LMD system (Table 1). The mass dispensing rates of each powder hopper were adjusted individually to achieve the stoichiometry of the target alloy, as a function of the hopping speed. Powders in the two containers were mixed and transported by an argon gas stream to the LMD nozzle (Fig. 1a). The dispensed rate of each powder batch was calibrated, and a linear relation between hopper speed and dispensed mass was established, so that reproducibility could be achieved (Fig. 1b). Samples (deposits) with the shape of small bricks (Fig. 1c) and approximate dimensions of 30 × 15 mm were produced. The total mass dispense rate was kept constant, resulting in a similar mass for all fabricated samples.

The structure of the deposited samples was characterized in the as-received samples and after heat-treatments by analytical SEM and powder x-ray diffraction (XRD), while the mechanical properties were evaluated with a Vickers microhardness tester. Based on the recent work of Yang et al (Ref 16) who studied the same alloy composition, two heat treatment menus
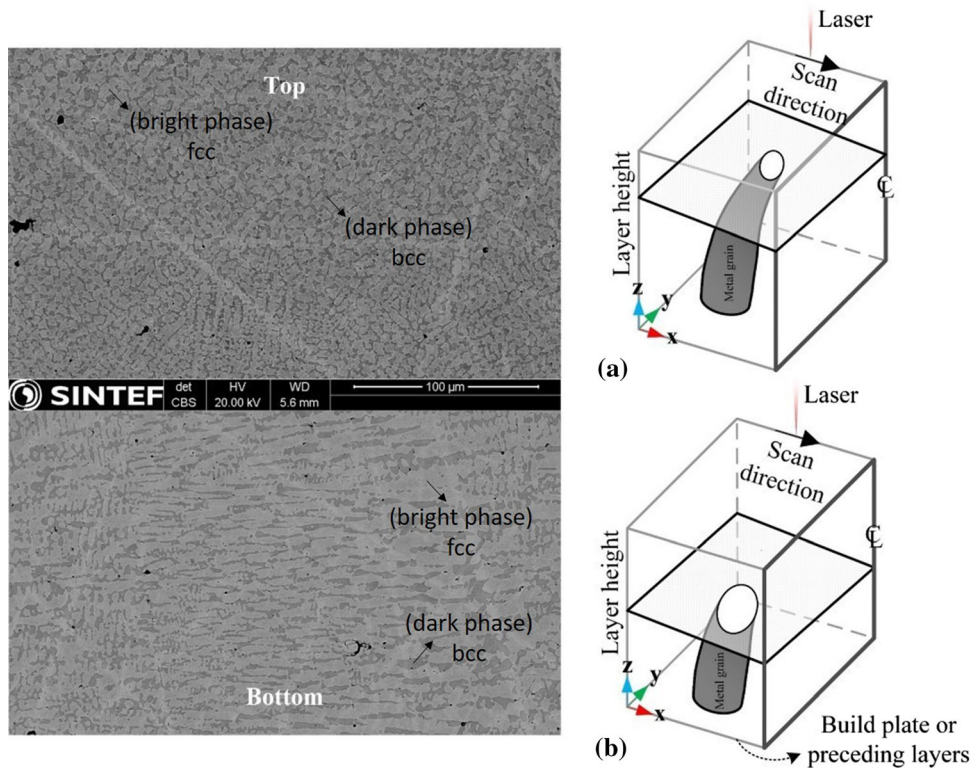
Figure 4 The microstructure of the $Fe_{28.1}Co_{28.1}Ni_{28.1}Al_{7.8}Mn_{7.8}$ alloy (S9) at (a) the top and (b) bottom part of the melting pool, showing the difference in the grain morphology due to grain growth
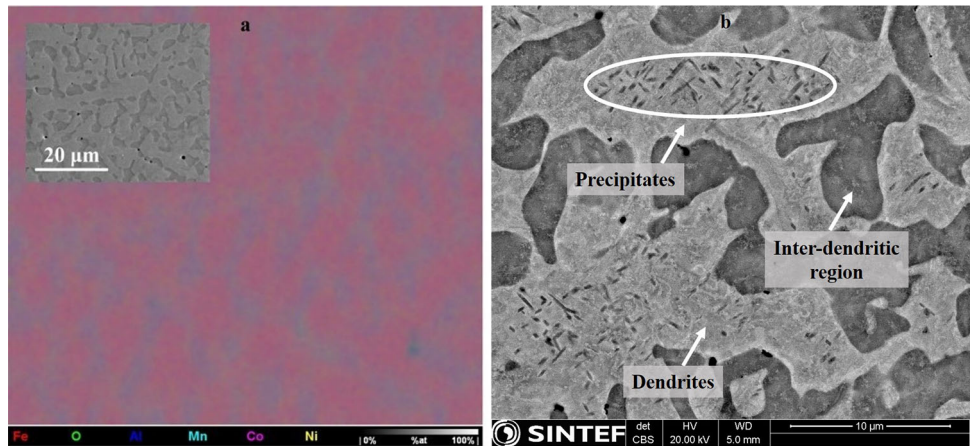

Figure 5 (a) EDS map for S9 (the relative SEM micrograph is inserted in the upper left corner) and (b) higher magnification SEM microstructural details for S9

were selected. The first one involved heating at 1000 °C for 10 h followed by furnace cooling. The second one included heating at 1000 °C for 3 h followed by water quenching. The two heat treatment procedures were selected in order to compare two extreme conditions; a longer exposure at high temperature followed by slow cooling (low cooling rate) and a shorter exposure at the same high temperature followed by rapid cooling (high cooling rate).

Cross-sectional samples were analyzed prior and after heat treatment, after etching with Nital in a Hitachi tabletop TM3000 SEM with a tungsten cartridge filament and an energy-dispersive detector (QUANTAX 70). Selected as-re-

ceived samples were also investigated via STEM, on an FEI Titan G2 60-300 kV instrument with an annular bright field (ABF) detector. EBSD measurements using a FEI Nova NanoSEM 650 were also performed for selected alloys, in order to investigate further their microstructural texture and grain size. A Rigaku MiniFlex600 system using Cu Ka radiation and fluorescence correction was used for the XRD measurements. The intensity accuracy verification was tested using the Silicon NIST 640d standard. Finally, a FM-700 Vickers microhardness tester from Future-Tech was used for the microhardness measurements performed with two different dwell times, 5 s and 20 s, and three different loads 0.025 kg,
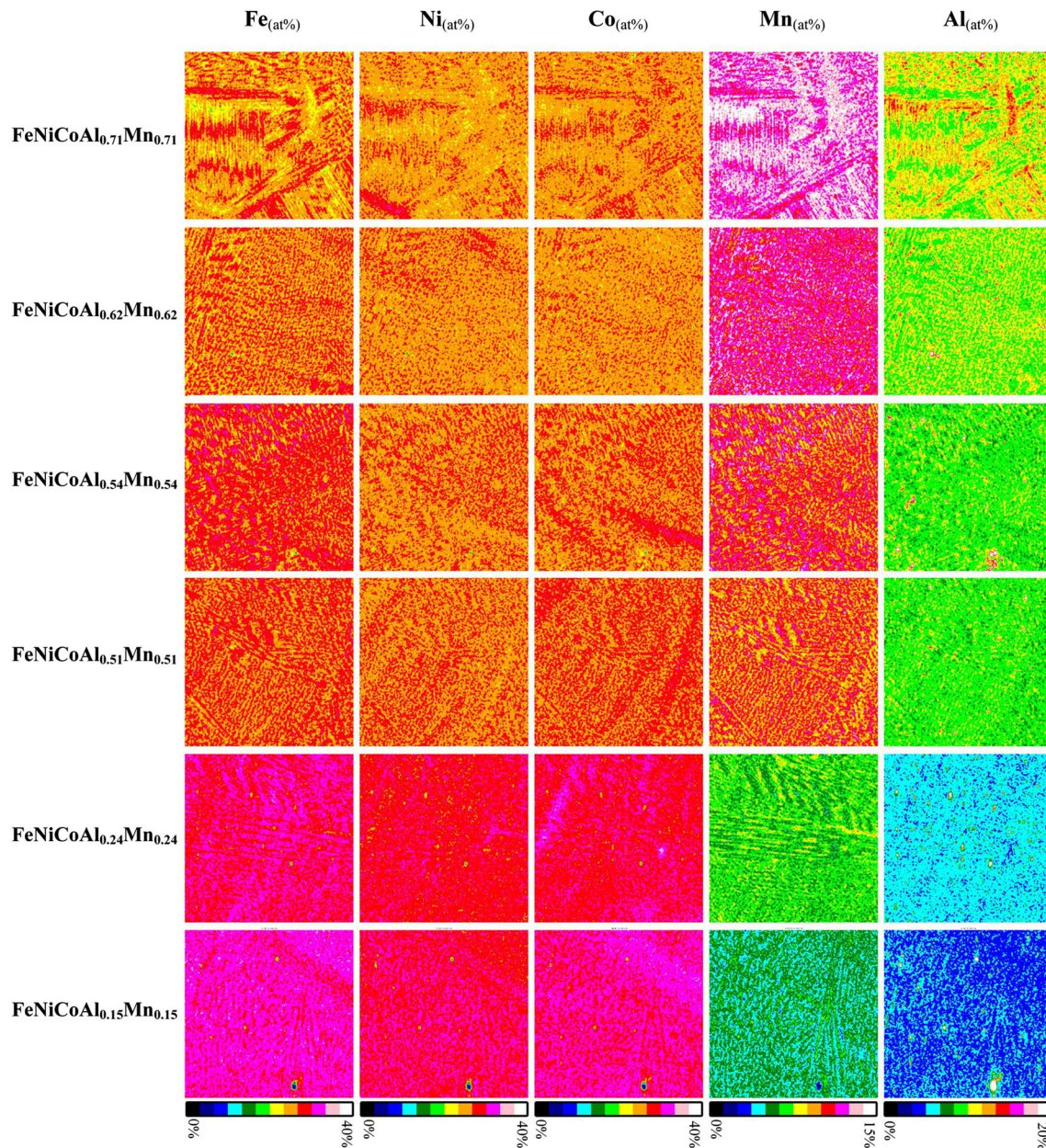
Figure 6 EDS maps for S9-S14

0.5 kg and 2 kg. Five measurements per sample per testing condition were performed, and the standard deviation was used to define the error bars.

3. Results

3.1 Feedstock Characterization

Figure 2 shows images of the elemental powders used to produce samples via LMD, having different size and shape distributions prior to sieving. The contents of light elements in the initial powders were not determined. However, according to EDS, all elemental powders showed a purity level of more than 99%. Disparity was observed in terms of size distribution and morphology of the original powder particles. Therefore, each powder batch was sieved to narrow particle size within the 35–200 μm range, in order to improve its flow characteristics. The powder particle morphology did not seem to affect the mass dispensing property in the vibrating hoppers. Among the batches, Mn and Al powders were the least flowable ones, due to the polymorphic shape and variable aspect ratio of the particles. After blending, an improved flowability was achieved, as the blended spherical particles from other elements should have presumably mitigated the poor flow properties of the non-spherical particles.

3.2 Microstructural Evolution in FeCoNiAl$_x$Mn$_x$ Systems

Figure 3 shows the comparative XRD patterns of all alloys synthesized in their as-received condition. The samples of highest Al and Mn contents (e.g., S1) mostly form a bcc-based ordered lattice. In samples with intermediate Al and Mn
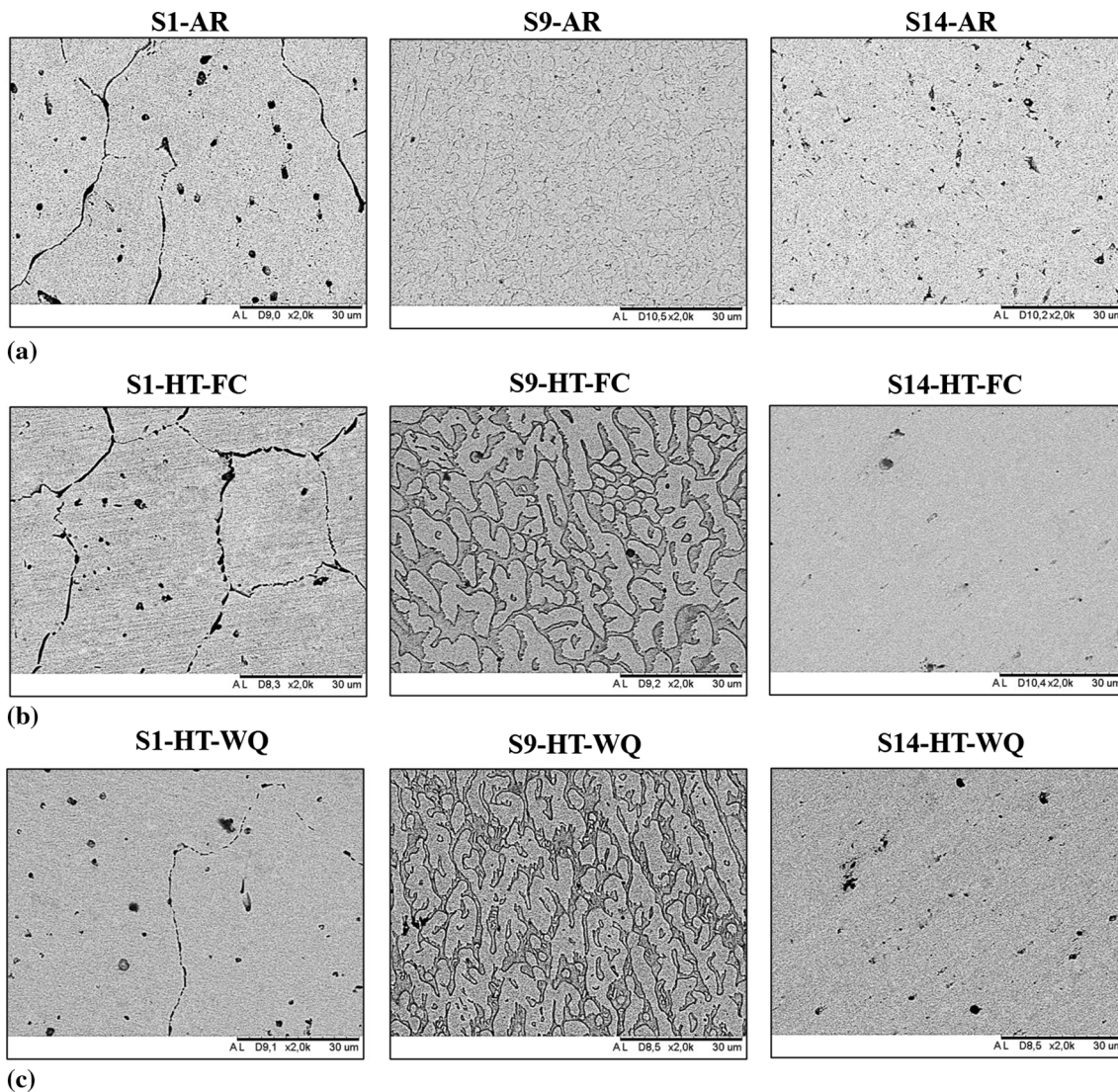
Figure 7 Micrographs for S1, S9 and S14 in (a) the as-received condition (AR), (b) after heat treatment followed by furnace cooling (HT-FC) and (c) after heat treatment followed by water quenching (HT-WQ)

contents, a coexistence of both a bcc-based structure with a fcc-type having a lattice parameter of a = 3.6 Å is observed, while in samples with low percentages of Al and Mn (e.g., S14), the fcc-type structure gradually dominates in the microstructure.

In order to understand the effects of the LMD process on the microstructural morphology, metallographic cross sections were prepared and observed via SEM. In general, the alloys exhibited a columnar cellular/dendritic configuration, which tends to form more equiaxed patterns as the Al-Mn content decreases.

Figure 4 shows the microstructure of S9, which is a representative sample as it exhibits all microstructural features that are present in various fractions in the samples, including the two main phases: the ordered bcc phase rich in Al and Mn and the fcc phase with lower Al and Mn contents. The microstructure of the upper part of the deposited block is influenced by the rapid cooling of the final melt pool, and this results in a finer cellular-like configuration (Fig. 4a). On the contrary, coarse columnar grains are formed in the underlying layers as a result of lower cooling rates, as captured in Fig. 4b.

These dendritic columnar grains exhibit a growth along the building direction.

The columnar grains, growing in a single direction at the bottom of the melt pool, form due to a large temperature gradient generated at this site (Ref 17). On the contrary, at the top of the melt pool, the basic microstructural features are influenced by high cooling rates that restrain the growth of crystals along a preferential crystal orientation.

The microstructure of the representative S9 alloy is composed of two different phases, appearing as bright and dark regions. EDS mapping (Fig. 5a) has shown that the Al-rich phase forms at the inter-dendritic regions, while the Fe-rich regions correspond to the dendrites. The compositions of these two regions derived from EDS point analysis are shown in Table 1. A closer examination of the microstructure showed that Al- and Mn-rich precipitates mostly form within the dendrites (Fig. 5b).

EDS mapping for S9-S14 (Fig. 6) further revealed that Fe, Co and Ni are in general homogeneously distributed in the dendritic regions. Especially for S9, a characteristic needle-like
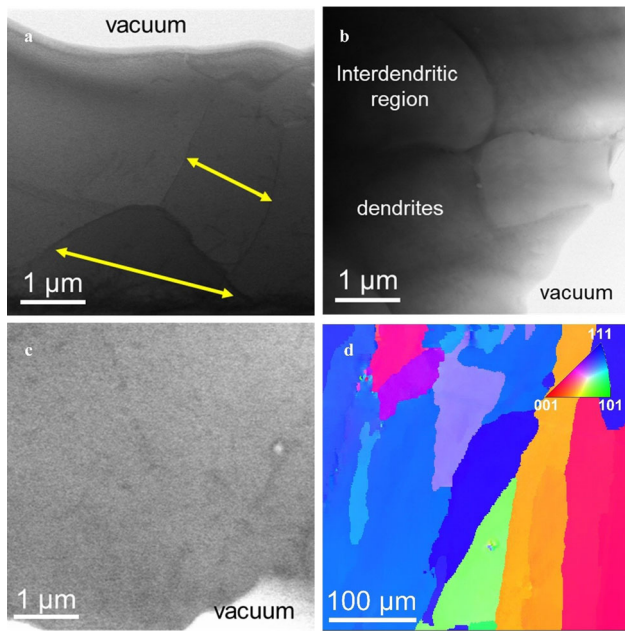
Figure 8 Low-magnification Annular Bright Field (ABF)-STEM images for (a) S1 (grain boundaries are annotated by arrows), (b) S9 and (c) S14 samples and (d) inverse pole figure (IPF-Z) map from a selective area of S14 sample, showing large grain size

morphology that could possibly be correlated with a Widmanstätten pattern is spotted.

SEM (Fig. 7), TEM (Fig. 8a-c) and EBSD (Fig. 8d) imaging of S1, S9 and S14 revealed the following tendencies: The microstructure of the as-received sample containing the highest atomic percentages of Al and Mn (S1) consists of large grains around 30–100 μm (Fig. 7a), while the presence of smaller sub-grains of the order of around 2 μm is also detected (Fig. 8a). Reduced Al and Mn contents (S9 and S14) lead to morphologies with grains over 100 μm up to the range of some mm (Fig. 7a). In order to further verify this observation, Fig. 8 shows low-magnification Annular Bright Field (ABF)-STEM images for S1, S9 and S14, respectively. S1 exhibits sub-grains of 2–3 μm size (grain boundaries are annotated by arrows, see Fig. 8a). S9 shows clear interfaces between dendritic and interdendritic regions, while the microstructure of S14 exhibits larger grains without obvious a sub-grain structure. EBSD mapping for S14 further verified the presence of larger grains in this sample (Fig. 8d).

Figure 7(b) shows that heat treatment did not alter the microstructural features of the alloys in a very significant way. The most obvious changes were observed for S1, where an increase in hardness was observed upon both heat treatment conditions. This is attributed mainly to the destruction of the cellular/dendritic solidification structure (Fig. 7a) and the formation of equiaxed grains (Fig. 7b) in the case of furnace cooling. This was well aligned with the increased hardness for S1 after heat treatment. A slightly coarser grain size (Fig. 7c) was observed after water quenching, and this agrees with the slightly reduced hardness after WQ as compared to the FC sample. Samples with lower Al and Mn contents (S9 and S14), on the contrary, seem to have maintained their microstructural texture in both as received and heat-treated conditions.

The slightly lower hardness of the heat treated, and water quenched sample as compared to the furnace cooled sample is attributed to the time effect in the conversion of the solidification structure. The formation of equiaxed grains upon heat treatment was facilitated by the synergistic action of the relatively high treatment temperature and duration, further assisted by a prolonged furnaced cooling. It seems that water quenched had as an effect an incomplete destruction of the solidification structure due to shorter exposure at a high temperature. The heat treatment conditions were inadequate to break the solidification structures of the lower Al and Mn content samples (S9 and S14), and thus, heat treatment had no effect in the hardness of these alloys.

3.3 Mechanical Properties of FeCoNiAl$_x$Mn$_x$ Systems

Microhardness values of all as-received and heat-treated samples were obtained under different loads and dwell times (Fig. 9). Table 2 presents the high correlation values between these measurements. The correlation coefficient is used to measure the strength of the relationship between two variables. A correlation value of 1 denotes perfect matching of the data, while a value of 0 represents no correlation between the two datasets. As it can be seen, despite the observed differences, the data obtained under different loading conditions and dwell times are still highly correlated. The lowest correlation value is detected between the HV5/5sec and the HV5/20sec dataset, which is still above 96%.

The as-received samples showed a clear increase in hardness for all experimental conditions with increasing Al and Mn content, as illustrated in Fig. 9. In this context, S1 with the highest at.% in Al and Mn showed the maximum hardness values in all testing conditions, while S14, having the lowest Al and Mn content exhibited the lowest hardness values. A reversed sigma-type curve characterizes the variation of hardness with respect to composition for measurements performed at the shortest dwell time (5 sec), while for measurements with longer dwell time (20 sec), the hardness varies almost linearly as a function of composition.

The observed differences in hardness when measured at different loads and/or dwell times could be attributed to the actual material response. Relaxation of the material after indentation can be a source of error for the registered hardness values. According to early studies summarized by Shahdad et al. (Ref 18), composite materials can show such a behavior. If the elastic relaxation is high, the indentation area will seem smaller upon unloading. Depending on the size and distribution of dispersed hardening particles, smaller indentation areas caused by low loading levels or short dwelling times are more sensitive to material spring-back or relaxation. This is observed for samples S1 to S5 under 25 gr load and 5 sec dwell time. However, this is not observed under 20 sec loading. Such an observation suggests that the microstructures of samples with higher Al and Mn contents probably contain nano-phased particles, which increase the relaxation of the material when indentation area is small. The study of such nano-phased particles is a scope for further investigations of these materials.

To a certain extent, it is generally accepted that the increase in hardness of HEAs is attributed to solid solution strengthening manifested by either direct or indirect interactions between solute atoms and dislocations. However, the formation of random solid solutions is in practice difficult to achieve in HEAs, due to the initial solid/liquid partition, the enthalpy driven phase reordering, or to separation phenomena that are commonly detected in many systems. Thus, the impact of such
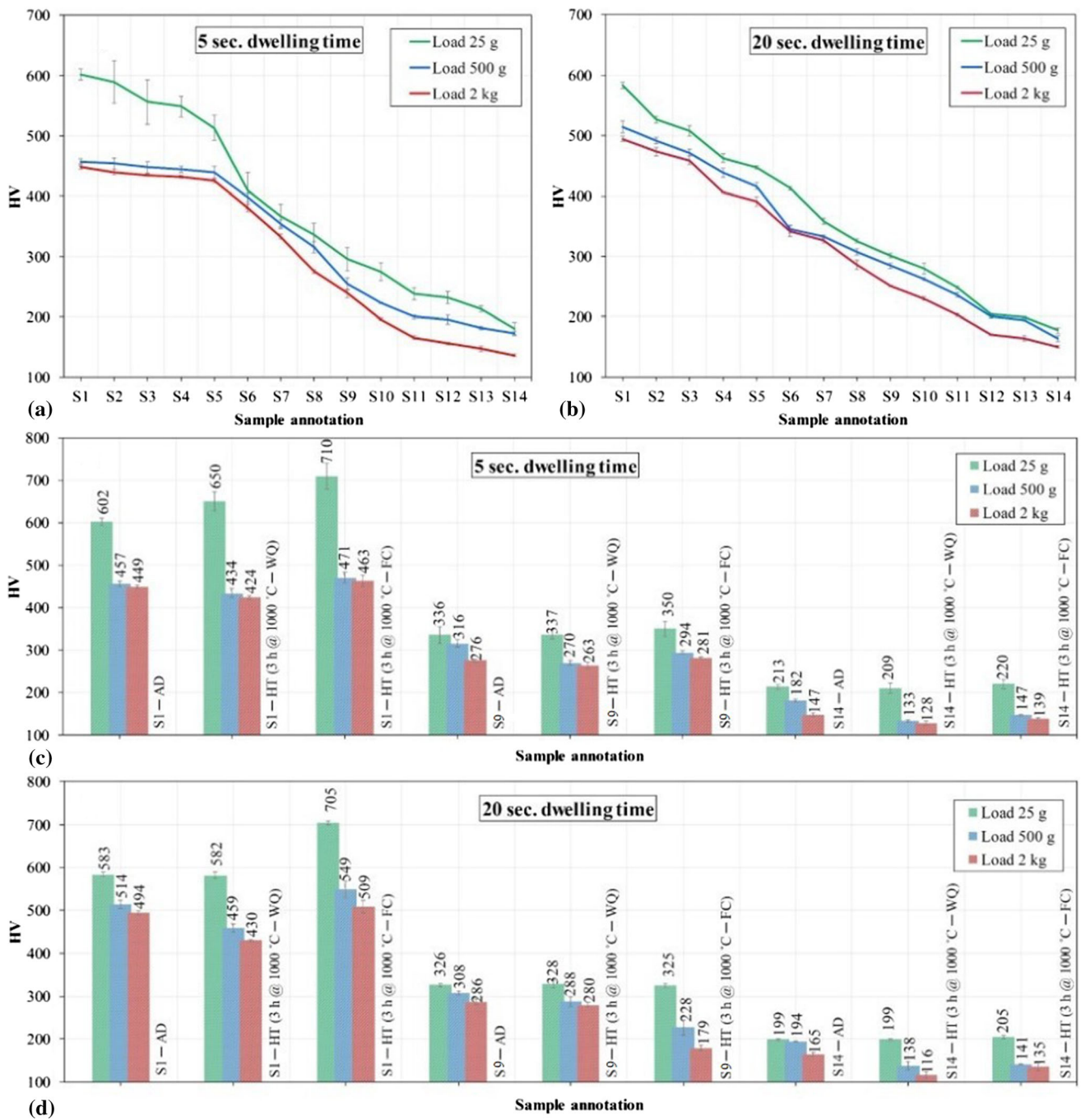
Figure 9 Vickers microhardness values of the as-deposited (AD), heat treated in furnace cooled (FC) and water quenched (WQ) conditions (a) shows the hardness for all as-deposited samples under 5 sec. indentation load dwelling time and (b) under 20 sec. dwelling time, (c) and (d) are comparing the results in terms of effect of heat treatment on three different samples and under two indentation load dwelling time, respectively

local chemical ordering on dislocation motion becomes a crucial issue. In the present work, it is suggested that structural ordering influences the hardness variations to a large extent. The ordered bcc phase, dominating the microstructure of the samples with high Al and Mn content, is the main factor for the increased hardness measured in these samples.

Structure ordering can be directly connected to many thermodynamic and geometric parametric values. In particular, calculations of the difference in the enthalpy of mixing for all compositions clearly show that S1 has the most negative value ($\Delta H_{mix,S1} = -17$ kJ/mol), while for S14, the aforementioned

value increases to $\Delta H_{mix,S14} = -7$ kJ/mol. This means that the formation of ordered intermetallic phases is more favorable for S1, whereas for S14, the reduced tendency for ordering (less negative ΔH_{mix}) and the presence of both ordered and disordered phases are reflected by a drop in hardness.

Moreover, the presence of precipitates is most likely to be an additional reason for the increased hardness, while the grain size also influences the hardness variations, since the presence of smaller grain sizes and/or the sub-grains reflect the increased hardness for S1 as compared to the rest of the samples, where larger grains were detected.

Table 2 Correlation values of the different hardness measurements (under different loads and dwell time values)

	HV0.25/5sec	HV5/5sec	HV20/5sec	HV0.25/20sec	HV5/20sec	HV20/20sec
HV0.25/5sec	1	0.975	0.977	0.986	0.992	0.989
HV5/5sec	0.975	1	0.998	0.968	0.965	0.974
HV20/5sec	0.977	0.998	1	0.972	0.969	0.976
HV0.25/20sec	0.986	0.968	0.972	1	0.994	0.995
HV5/20sec	0.992	0.965	0.969	0.994	1	0.996
HV20/20sec	0.989	0.974	0.976	0.995	0.996	1

Additionally, all samples in all testing conditions show higher microhardness values at a low load exhibiting thus a normal indentation size effect (ISE) (Ref 19). Materials with normal ISE are normally not prone to plastic deformation, and the phenomenon is attributed to intrinsic structural factors, such as work hardening during indentation, load to initiate plastic deformation, elastic resistance and mixed elastic/plastic deformation response of the material (Ref 20–22). This is aligned with the large difference between the microhardness values obtained upon indentation with low and higher loads for the high at.% Al and Mn samples, e.g., S1 to S5. The microstructure of these samples is dominated by the presence of the bcc-ordered phase. On the contrary, samples with decreasing Al and Mn content (samples toward S14) exhibit a less intense normal ISE. The microstructure of these samples is dominated by an increasing fraction of the disordered fcc phase, which is more susceptible to plastic deformation owing to more active slip systems.

Finally, the effect of the heat treatment on the hardness of the alloys does not seem to be drastic, with the exception of S1 in both dwell times. When applying the lowest load of 25 g, a sharp increase from 602 to 710 HV is observed for S1 for a dwell time of 5 sec, while the same trend is followed for a 20 sec dwell time (increase from 583 to 705 HV). The heat-treated S9 and S14 show a moderate strengthening trend for the lowest load of 25 g. This upward trend does not seem to be clear when higher loads of 500 g and 2 kg are applied, for the three samples. In these cases, the hardness seems to be either unaffected or to slightly decrease in all samples for all dwell times in both heat-treated conditions.

The impact of Al and Mn content in the hardness values of the systems was also analyzed using artificial neural network model (ANN), where the atomic concentration of the five elements is selected as input factors and the measured hardness values under various conditions are set as responses. The best results in the structure of the ANN and training levels yielding about 92% and 97% accuracy (R^2) for training and validation, respectively, are shown in (Fig. 10a). Two hidden training layers were introduced. The first layer is a three-level TanH type, and the second layer is a linear type. Surface profiler illustration is used in Fig. 10b, c to present the effect of Al and Mn content on the 0.025 kg indentation load data. The selected chemical compositions belong to S1 and S14 in Fig. 10(b, c), respectively.

By creating the hardness profile as a function of the constituent elements concentration, the positive role of Al and Mn is highlighted. The same trend was also observed for all hardness testing conditions (e.g., varying time and loads), but for brevity reasons, these results are not illustrated here. Instead, the respective Python code for the developed ANN is provided in the supplementary file for further modeling of the results by the readers, without requiring access to the data points.

4. Conclusions

A series of HEAs with variable FeCoNiMnAl compositions were successfully produced by LMD. The microstructures showed a strong dependence on the processing conditions and solidification parameters governing constitutional undercooling. The latter triggered a switch in microstructural morphology from columnar dendritic to equiaxed dendritic, from the bottom to the top of the melt pool. A variation of the mechanical properties with composition was observed in the form of an
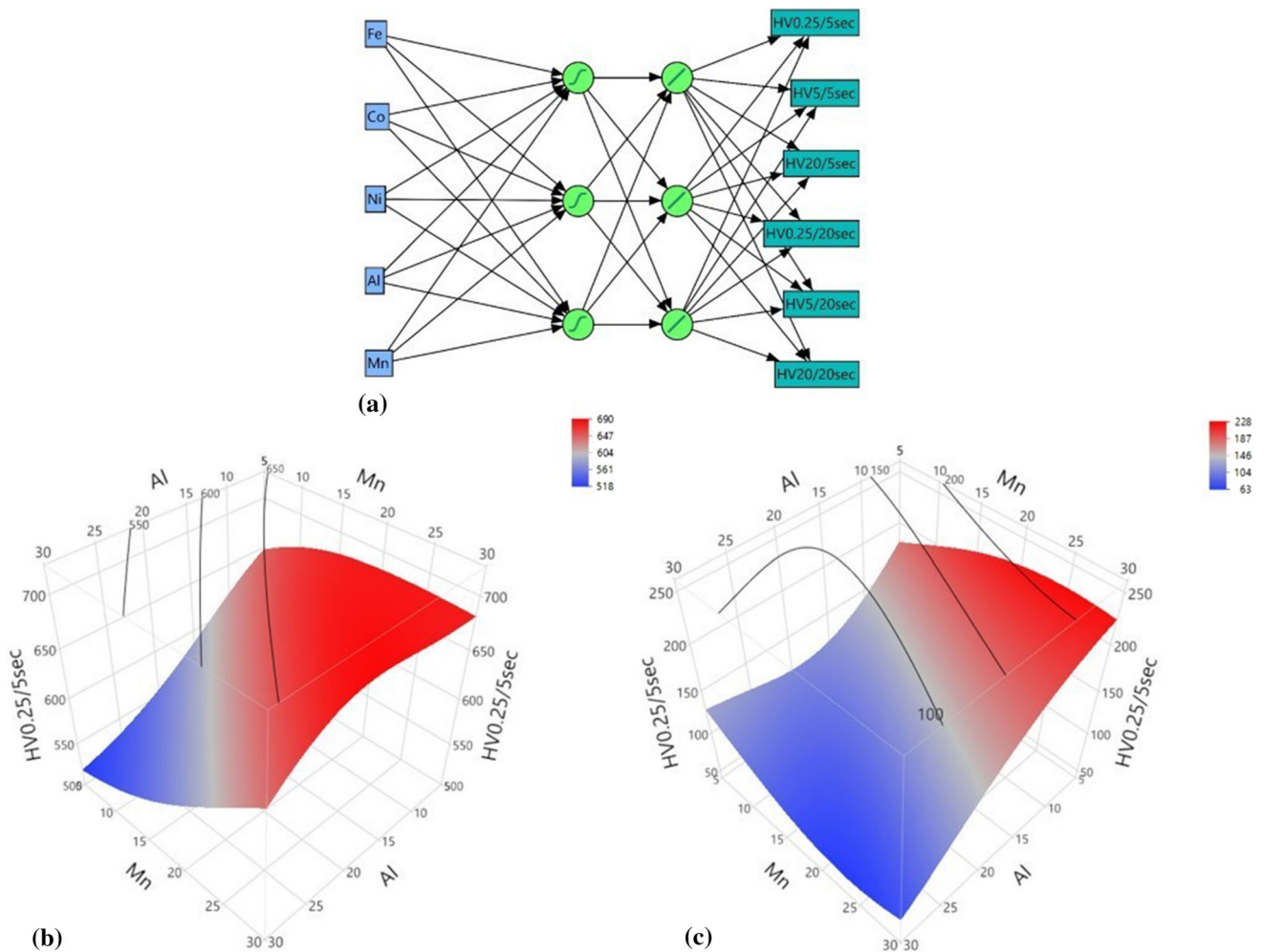
Figure 10 (a) Neutral network diagram, and surface profile predictions regarding the effect of Al and Mn variation on the hardness of (b) $Fe_{10.9}Co_{10.9}Ni_{10.9}Al_{33.6}Mn_{33.6}$ (S1) and (c) $Fe_{32.3}Co_{32.3}Ni_{32.3}Al_{1.6}Mn_{1.6}$ (S14) alloy compositions

inverse "S" shape of microhardness values vs composition. The increase in microhardness with increasing Al and Mn content was attributed mainly to structural ordering, solid solution strengthening and grain size variations among the different samples. Finally, the use of artificial neural network modeling establishes the structure–hardness relationship and highlighted the effect of the Al and Mn content on the hardness evolution.

References

1. Y. Zhang, T.T. Zuo, Z. Tang, M.C. Gao, K.A. Dahmen, P.K. Liaw and Z.P. Lu, Microstructures and Properties of High-entropy Alloys, *Prog. Mater. Sci.*, 2014, **61**, p 1–93.

2. Y. Jien-Wei, Recent Progress in High Entropy Alloys, *Ann. Chim. Sci. Mat.*, 2006, **31**(6), p 633–648.

3. J.W. Yeh, S.K. Chen, S.J. Lin, J.Y. Gan, T.S. Chin, T.T. Shun, C.H. Tsau and S.Y. Chang, Nanostructured High-entropy Alloys with Multiple Principal Elements: Novel Alloy Design Concepts and Outcomes, *Adv. Eng. Mater.*, 2004, **6**(5), p 299–303.

4. W. Zhang, P.K. Liaw and Y. Zhang, Science and Technology in High-entropy Alloys, *Sci. China Mater.*, 2018, **61**(1), p 2–22.

5. E.P. George, D. Raabe and R.O. Ritchie, High-entropy Alloys, *Nat. Rev. Mater.*, 2019, **4**(8), p 515–534.

6. M.H. Tsai and J.W. Yeh, High-entropy Alloys: a Critical Review, *Mater. Res. Lett.*, 2014, **2**(3), p 107–123.

7. X. Yan and Y. Zhang, Functional Properties and Promising Applications of High Entropy Alloys, *Scripta Mat.*, 2020, **187**, p 188–193.

8. M.C. Gao, J.W. Yeh, P.K. Liaw and Y. Zhang, *High-Entropy Alloys*, Springer International Publishing, Cham, 2016

9. S. Gorsse, J.P. Couzinié and D.B. Miracle, From High-entropy Alloys to Complex Concentrated Alloys, *C. R. Phys.*, 2018, **19**(8), p 721–736.

10. H.S. Oh, S.J. Kim, K. Odbadrakh, W.H. Ryu, K.N. Yoon, S. Mu, F. Körmann, Y. Ikeda, C.C. Tasan and D. Raabe, Engineering Atomic-level Complexity in High-entropy and Complex Concentrated Alloys, *Nat. Commun.*, 2019, **10**(1), p 1–8.

11. P. Chen, S. Li, Y. Zhou, M. Yan and M.M. Attallah, Fabricating CoCrFeMnNi High Entropy Alloy via Selective Laser Melting in-situ Alloying, *J. Mater. Sci. Technol.*, 2020, **43**, p 40–43.

12. P. Chen, C. Yang, S. Li, M.M. Attallah and M. Yan, In-situ Alloyed, Oxide-Dispersion-Strengthened CoCrFeMnNi High Entropy Alloy Fabricated Via Laser Powder Bed Fusion, *Mater. Des.*, 2020, **194**, p 108966-1–108966-9

13. V.V. Popov, A. Katz-Demyanetz, A. Koptyug and M. Bamberger, Selective Electron Beam Melting of $Al_{0.5}CrMoNbTa_{0.5}$ High Entropy Alloys Using Elemental Powder Blend, *Heliyon*, 2019, **5**, p 01188-1–01188-16

14. Y. Dong, Y. Li, S. Zhou, Y. Zhou, M. Dargusch, H. Peng and M. Yan, Cost-Affordable Ti-6Al-4V for Additive Manufacturing: Powder Modification, Compositional Modulation and Laser In-situ Alloying, *Addit. Manuf.*, 2021, **37**, p. 101699-1–101699-9

15. M.H. Tsai, J.H. Li, A.C. Fan and P.H. Tsai, Incorrect Predictions of Simple Solid Solution High Entropy Alloys: Cause and Possible Solution, *Scripta Mater.*, 2017, **127**, p 6–9.

16. C. Yang, J. Zhang, M. Li and X. Liu, Soft-magnetic High-entropy AlCoFeMnNi Alloys with Dual-phase Microstructures Induced by Annealing, *Acta Metall. Sinica-Eng.*, 2020, **33**, p 1124–1134.

17. D. Gu, Q. Shi, K. Lin and L. Xi, Microstructure and Performance Evolution and Underlying Thermal Mechanisms of Ni-based Parts Fabricated by Selective Laser Melting, *Addit. Manuf.*, 2018, **22**, p 265–278.

18. S.A. Shahdad, J.F. McCabe, S. Bull, S. Rusby and R.W. Wassell, Hardness Measured with Traditional Vickers and Martens Hardness Methods, *Dent. Mater.*, 2007, **23**(9), p 1079–1085.

19. J. Petrík, On the Load Dependence of Micro-hardness Measurements: Analysis of Data by Different Models and Evaluation of Measurement Errors, *Arch. Metall. Mater.*, 2016, **61**(4), p 1819–1824.

20. K. Sangwal, B. Surowska and P. Błaziak, Analysis of the Indentation Size in the Microhardness Measurement of Some Cobalt-based Alloys Materials, *Mater. Chem. Phys.*, 2002, **77**(2), p 511–520.

21. K. Sangwal, On the Reverse Indentation Size Effect and Microhardness Measurement of Solids, *Mater. Chem. Phys.*, 2000, **63**(2), p 145–152.

22. X.J. Ren, R.M. Hooper and C. Griffiths, Indentation Size Effect in Ceramics: Correlation with H/E, *J. Mater. Sci. Lett.*, 2003, **22**(15), p 1105–1106.